LASER & PHOTONICS REVIEWS
www.lpr-journal.org

Bandwidth Enhancement of Epsilon-Near-Zero Supercoupling with Inverse-Designed Metamaterials

*Pengyu Fu, Peihang Li, and Yue Li**

Epsilon-near-zero (ENZ) materials exhibit unique electromagnetic properties that enable efficient wave transmission through channels of arbitrary geometry, which is known as ENZ supercoupling or tunneling. However, the supercoupling effect is typically confined to an inherent narrow bandwidth, which significantly restrict its practical applications. In this paper, a feasible method is proposed that enhanced the bandwidth of ENZ supercoupling. By optimizing the structure of an inverse-designed pixel metamaterial inserted into the ENZ channel, multiple Fabry-Perot (FP) modes are properly regulated and coupled, facilitating multimode superposition to enhance the bandwidth for high-efficiency signal transmission in ENZ channels with arbitrary geometry. Furthermore, a prototype is constructed at microwave frequency to validate the performance of the proposed method, which opens new avenues for the development of broadband and geometry-independent electromagnetic devices with the benefit of ENZ materials.

1. Introduction

Materials with extreme permittivity and permeability have received widespread attention for their transformative applications in photonics and electronics due to their unique electromagnetic characteristics. Epsilon-near-zero (ENZ) materials, characterized by near-zero permittivity, cause the wavelength within the material to approach infinity, enabling precise control of electromagnetic waves in highly confined spaces.[1] Benefiting from these distinct properties, ENZ materials have been extensively studied and applied, facilitating advancements in various technologies.[2–4] In the communication system, ENZ-based antennas and waveguides can achieve high integration and efficiency.[5–10] Moreover, the ability to control multifrequency wave propagation also makes ENZ materials suitable for frequency-division multiplexing systems, thereby increasing data transmission capacity.[11,12] Additionally, the field enhancement properties of the ENZ materials enable the application in nonlinear optics.[13–15] Furthermore, ENZ materials also contribute to the creation of high-efficiency absorbers and analog computing devices.[16–18]

As one of the key applications of ENZ materials, electromagnetic waves can efficiently transmit through ENZ channels of arbitrary geometry, bypassing the reflection and scattering, which is known as the supercoupling or tunneling effect.[19–22] The supercoupling effect provides a promising foundation for highly compact, efficient, and flexible wave manipulation and transmission systems, and has been validated both in microwave and optical frequencies.[23–27] However, limited by the dispersion and losses inherent in ENZ materials, the supercoupling effect is only achieved over a narrow bandwidth, restricting its applications in real photonic and electronic systems.[28] To address this issue, numerous methods have been proposed. One approach to enhancing the supercoupling involves improving the efficiency of ENZ materials through modified doping methods.[29,30] Active ENZ materials have been studied to maintain low losses across a broader bandwidth.[31] Additionally, various studies have explored different techniques for tuning the resonant frequency of ENZ materials to achieve tunable ENZ supercoupling.[32–34] As an important approach, ENZ materials base on metacomposites enables a wide range of tunable characteristics in the microwave frequency band through techniques such as stacking and photo-induced adjustment, offering an effective solution for the practical application of ENZ supercoupling.[35] Furthermore, research has investigated the utilization of other modes, such as Fabry-Perot (FP) modes and gap plasmon modes, in conjunction with supercoupling modes to extend the bandwidth of the supercoupling effect.[36,37] Moreover, the concept of metamaterials offers an effective approach that enables unprecedented control over electromagnetic waves across wide applications,[38] such as wireless communication,[39,40] analog computing,[41,42] and silicon nanophotonics.[43,44] Benefiting from this, metamaterials also provide an effective way to improve the performance of ENZ materials. For instance, by inserting metastructures into a waveguide, negative elements with inverse dispersion properties can be realized, which is expected to achieve wideband matching of ENZ materials.[45] Besides, a wideband isotropic ENZ properties can be constructed by metamaterial with sophisticated periodic symmetric superlattice microstructure.[46] Furthermore, a multilayer metamaterial consisting of different high index dielectric slabs

P. Fu, P. Li, Y. Li
Department of Electronic Engineering
Tsinghua University
Beijing 100084, China
E-mail: lyee@tsinghua.edu.cn
Y. Li
Beijing National Research Center for Information Science and Technology
Beijing 100084, China

The ORCID identification number(s) for the author(s) of this article can be found under https://doi.org/10.1002/lpor.202402014

DOI: 10.1002/lpor.202402014

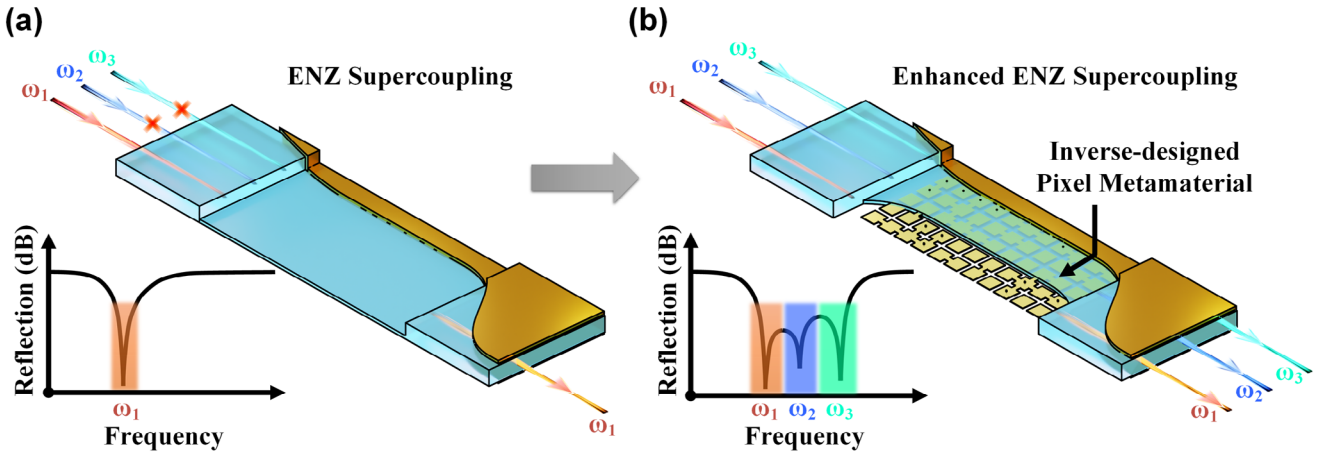

Figure 1. Bandwidth enhancement of ENZ supercoupling with inverse-designed metamaterial. a) Traditional ENZ supercoupling with a limited bandwidth. b) Enhanced ENZ supercoupling with wide bandwidth using the inverse-designed metamaterial inserted in the ENZ channel.

and films can be optimized for enhancement of the transmission, reflection, or loss characteristics of ENZ material.[47,48] Additionally, the absorption effect of ENZ materials can be significantly enhanced with metamaterials base on all-organic structures.[49]

In this work, we propose an inverse-designed pixel metamaterial approach to enhance the bandwidth of ENZ supercoupling. As shown in **Figure 1**a, a regular waveguide channel can achieve narrowband transmission at a single frequency point. By inserting a structurally optimized metamaterial within the ENZ channel, several FP resonant modes can be controlled to facilitate multimode superposition with supercoupling mode, result in a bandwidth enhancement of ENZ supercoupling, as shown in Figure 1b, even with arbitrary geometry. To validate, we have constructed a prototype at microwave frequency, demonstrating that this design effectively broadens the supercoupling bandwidth and has the potential in broadband and geometry-independent electromagnetic device applications.

2. Results

2.1. Pixel Metamaterials

As illustrated in Figure 1a, the supercoupling effect is confined to an effective ENZ waveguide, limiting its application in practical systems. Besides the ENZ supercoupling modes, FP modes in rectangular waveguides also allow total wave transmission at multiple discrete frequencies.[37] However, in conventional waveguide systems, there is a significant frequency gap between the ENZ mode and the FP modes, preventing effective superposition of multiple modes. To solve the problem, as shown in **Figure 2**a, an inverse-designed pixel metamaterial is proposed to enhance the bandwidth of supercoupling effect by enabling the superposition of ENZ and multiple FP modes. Figure 2b depicts the basic unit of the proposed pixel metamaterial, which comprises several metallic patches with a side length *a* and metallic vias with radius *r*. The connecting branches of width *s* and length *d* between adjacent patches can be optimized, as well as the metallic cylindrical structures between patches and waveguides. The position of the metamaterial is depicted in Figure 2c, indicating the center of the supercoupling channel. The sub-wavelength patches and metallic vias influence the electromagnetic waves propagating through the waveguide, thereby affecting the resonant frequencies of multiple modes within the supercoupling channel. So, the proposed metamaterial is convincingly high-potential for bandwidth enhancement of ENZ supercoupling.

2.2. ENZ Supercoupling Bandwidth Enhancement

Figure 3a shows an example of the proposed inverse-designed pixel metamaterial enhancing the bandwidth of supercoupling effect. When a typical supercoupling configuration is employed in a rectangular waveguide, an air-filled waveguide of thickness

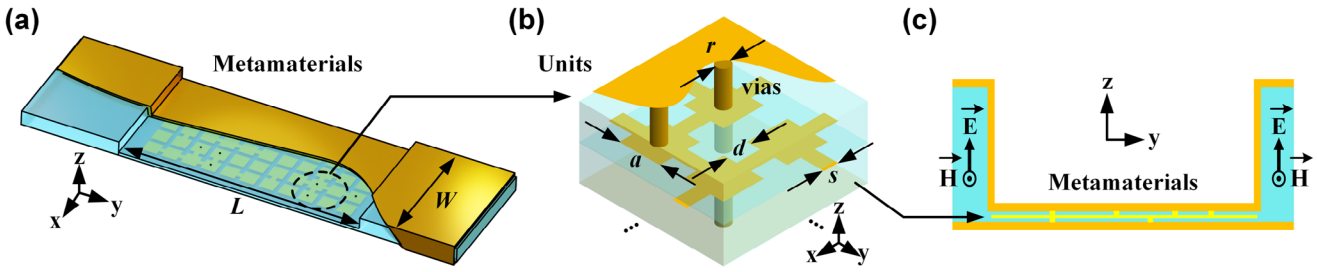

Figure 2. Pixel metamaterial inserted in ENZ supercoupling channel. a) Structure of the proposed bandwidth enhancement metamaterial. b) Basic units of metamaterials, including patches, branches and metalized vias, and the c) side view in supercoupling channels.

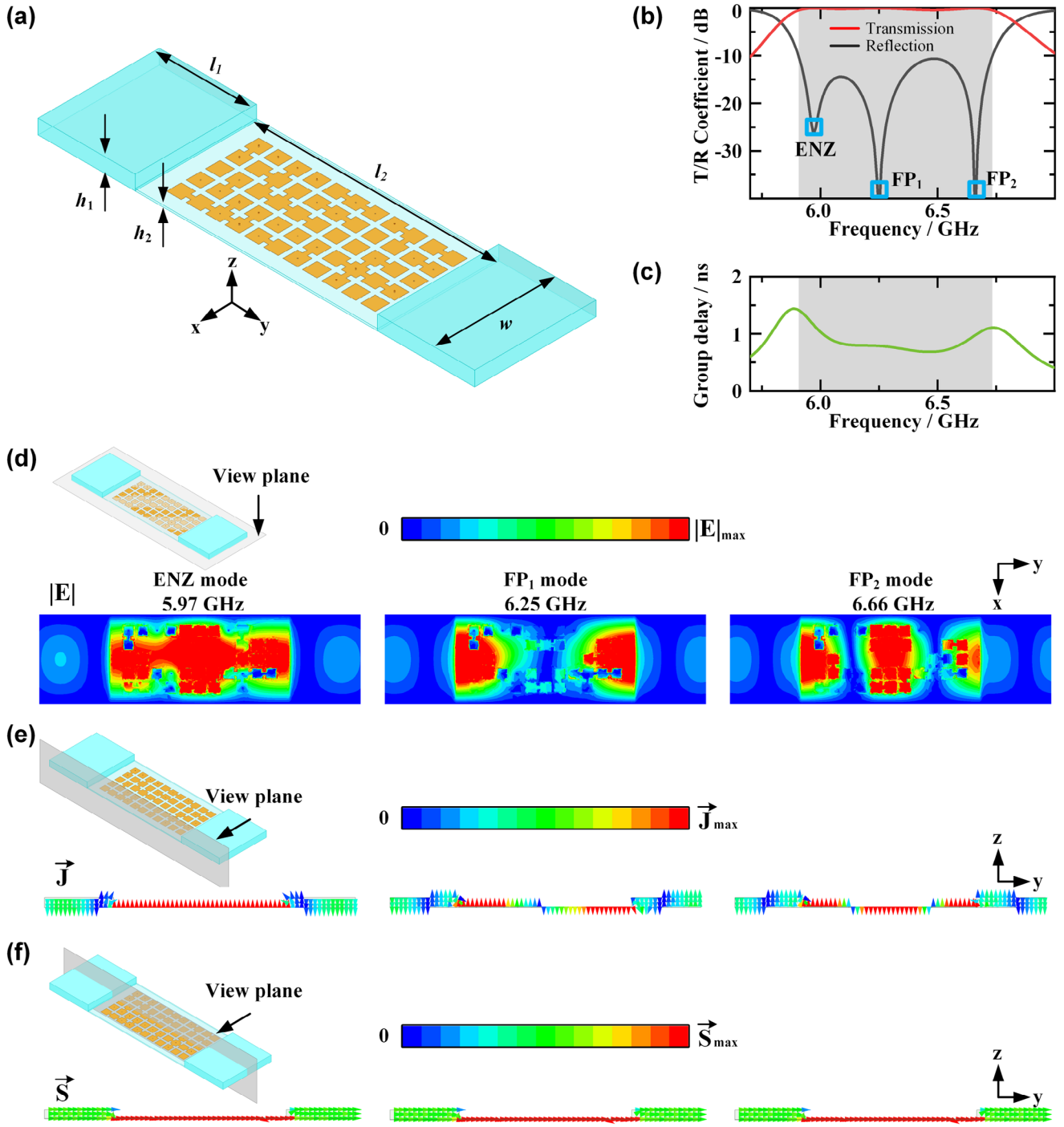

Figure 3. Multi-mode superposition and bandwidth enhancement based on inverse-designed metamaterials. a) The basic model of the metamaterial-insert supercoupling channel. b) The simulated transmission/reflection coefficients and c) the group delay of the inverse-designed metamaterial. d) Electric field distribution, e) surface current distribution, and f) Poynting distribution inside the supercoupling channel at three different resonates frequencies: 5.97, 6.25, and 6 .66 GHz.

h_2 and length l_2 is embedded between two dielectric-filled normal waveguides of width w and thickness h_1. At its cutoff frequency (wavelength of $2w$), the waveguide behaves as an ENZ material, exhibiting a narrowband supercoupling effect. By introducing an inverse-designed pixel metamaterial into the waveguide, multiple FP modes within the waveguide can be effectively controlled. As shown in Figure 3b, this modified configuration achieves a reflection coefficient below −10 dB and a transmission coefficient above −1 dB within the frequency range of 5.9–6.7 GHz, which significantly expands the bandwidth for

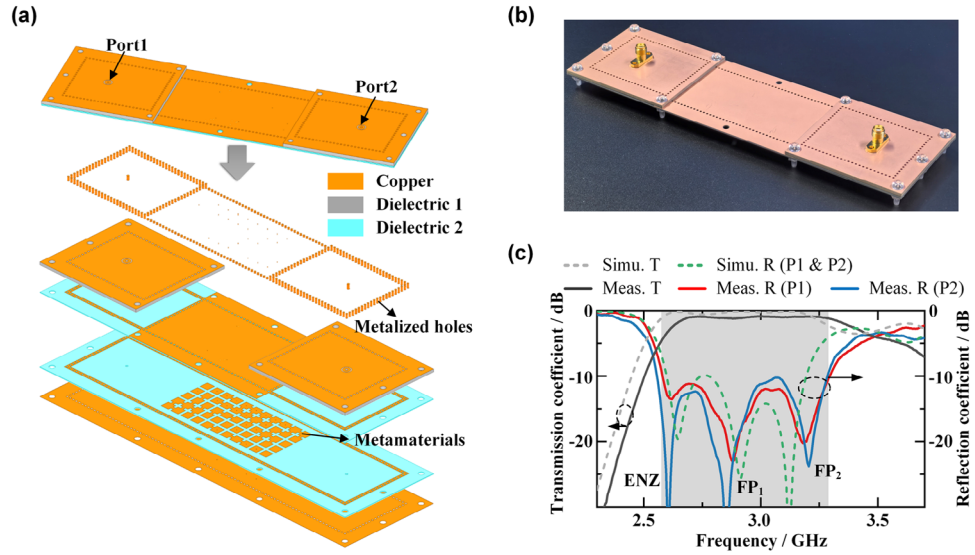

Figure 4. Prototype based on SIW method and measured results. a) A multi-layer structure schematic diagram of the proposed SIW-based prototype. b) Photo of the proposed prototype. c) The simulated and measured transmission and reflection coefficient of the proposed supercoupling channel.

supercoupling effect. Furthermore, Figure 3c exhibits that the group delay across the waveguide remains stable at ≈1 ns within the supercoupling bandwidth, demonstrating the stability of the proposed structure for broadband signal transmission.

Furthermore, the reflection coefficient in Figure 3b reveals three distinct resonant points, corresponding to the three modes within the broadband transmission. The electric field distributions at these resonant frequencies are illustrated in Figure 3d. At the first resonance point at 5.97 GHz, the electric field distribution in the y-direction is observed to be nearly uniform, suggesting the presence of a fundamental ENZ mode. At 6.25 GHz, the field exhibits a half-wavelength distribution along the y-direction, representing the first-order FP mode. While, at 6.66 GHz, a full-wavelength distribution represents the second-order FP mode in the supercoupling channel. Although the inverse-designed pixel metamaterial influenced the ideal mode profiles, the presence of these controlled resonant modes is clearly evident. Similarly, as Figure 3e shows, the surface currents on the side of metal waveguide provide intuitive representation of the mode distributions. The magnitude and direction of surface current display uniform, half-wavelength, and full-wavelength patterns at different resonant frequencies, further confirming the presence of ENZ, FP_1, and FP_2 modes. Finally, Figure 3f demonstrates the Poynting vector distribution within the supercoupling channel. At all the resonant frequencies, the Poynting vector remains uniformly distributed, which highlights the excellent broadband and lossless transmission characteristics of the proposed structure.

2.3. Experimental Verification

In the microwave to terahertz frequency range, substrate-integrated waveguide (SIW) is commonly used for integrated waveguide transmission. Here, we present an example based on SIW which demonstrates the bandwidth enhancement of ENZ supercoupling effect with inverse-designed metamaterial. As illustrated in **Figure** 4a, two dielectric materials with different permittivities are utilized to establish the cutoff frequency for supercoupling effect, and the inverse-designed pixel metamaterial is integrated at the center of the lower-permittivity region. Numerical simulations of this structure are conducted using Ansoft High-Frequency Structure Simulator (HFSS) with finite element analysis, which is shown by the dashed lines in Figure 4c. The results are closely consistent with those obtained from the metal rectangular waveguide, with three distinct resonant modes enabling broadband transmission through mode superposition.

Finally, as Figure 4b shows, a prototype of the proposed bandwidth-enhanced supercoupling based on metamaterial is fabricated with standard printed circuit board technology. Two surface-mount 50-ohm Sub-Miniature version A (SMA) connectors with probe structures are employed to excite the waveguide. Additionally, metal and plastic screws are used to secure the multilayer dielectric substrate. The reflection and transmission coefficients of the fabricated structure are measured with a vector network analyzer, which is depicted by the solid lines in Figure 4c. The experimental results align closely with the simulations, confirming that the resonant points correspond to the ENZ, FP_1, and FP_2 modes, thereby enabling broadband transmission. The bandwidth with a reflection coefficient below −10 dB and a transmission coefficient above −2 dB is 2.61–3.29 GHz (23%), meeting general wideband signal transmission requirements. These findings demonstrate that the proposed wideband supercoupling based on inverse-designed metamaterial can be easily integrated into existing waveguide systems, showing great potential for broadband waveguide devices.

3. Discussion

3.1. Process of Inverse Design

To achieve inverse design of metamaterials, a rapid optimization process using genetic algorithms (GA) and the method

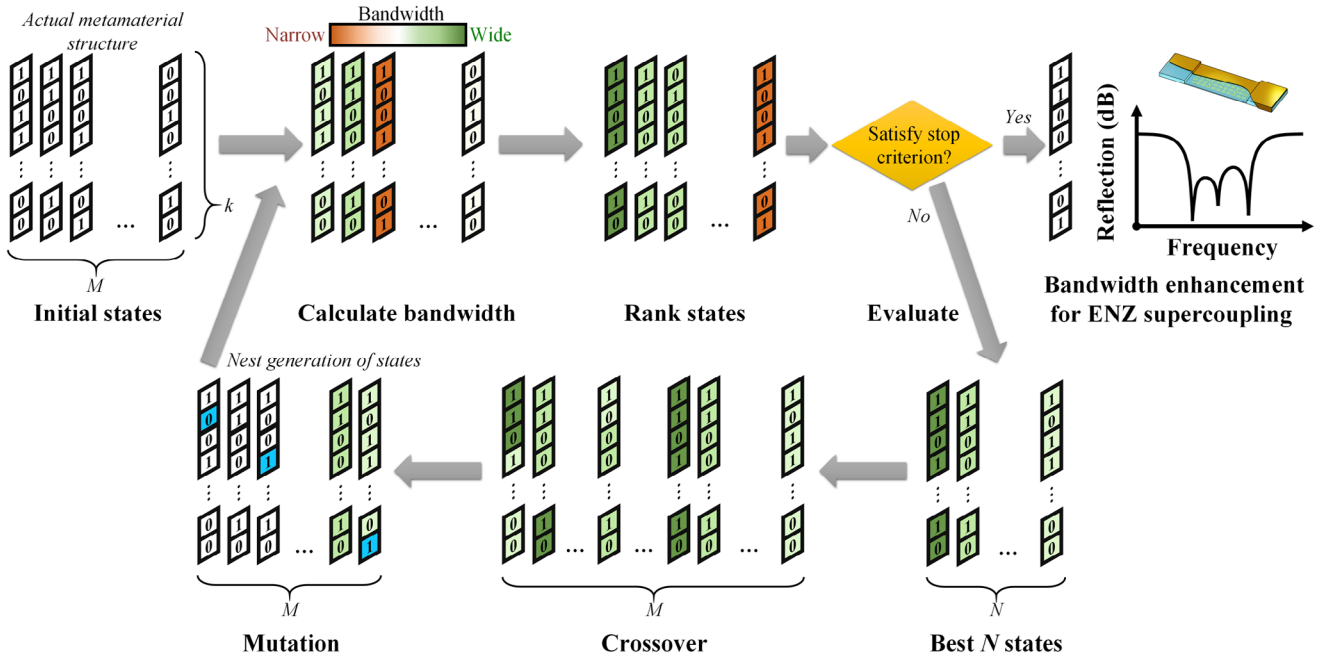

Figure 5. Inverse design process of pixel metamaterial based on GA optimization.

of moments (MoM) is employed to refine the structures for bandwidth enhancement of ENZ supercoupling. As illustrated in **Figure 5**, the optimization begins with randomly generated M initial states, and each state has a length k corresponding to the number of optimizable units, including the metalized vias and branches between patches. With the equivalent port circuit model derived from the MoM, the transmission and reflection coefficients for supercoupling can be quickly calculated across the frequency band of interest. Based on the desired metamaterial response, such as achieving a low reflection coefficient over a specific frequency range, the states are ranked and evaluated to determine whether the optimization objectives are satisfied. If the optimization goals are not met, the best N states will undergo crossover and mutation operations to generate a new generation, which is recalculated and reevaluated. This iterative process continues until the optimal response is obtained with the ENZ supercoupling bandwidth enhancement.

3.2. Transmission with Arbitrary Geometry

Benefitting from the uniform field properties in ENZ materials, conventional ENZ supercoupling waveguides can be flexed into arbitrary geometry without compromising performance, showing significant potential for signal transmission in complex structures. Furthermore, the performance of the proposed broadband supercoupling, powered by inverse-designed metamaterials, is evaluated for different geometric states. Without loss of generality, **Figure 6a** depicts a waveguide folded at a right angle, while Figure 6b shows a waveguide with a sharper, triple-folded state. Simulation results for both geometry states are shown in Figure 6c, which illuminate that high transmission and low reflection coefficients are maintained in a wide bandwidth consistent with the original state. Besides, aside from minor dispersion, the frequencies of the three resonant modes remain nearly identical to those of the original state, which means the resonant modes regulated by the metamaterial are maintained with different geographies. This finding highlights the potential of the proposed metamaterial-based broadband supercoupling approach

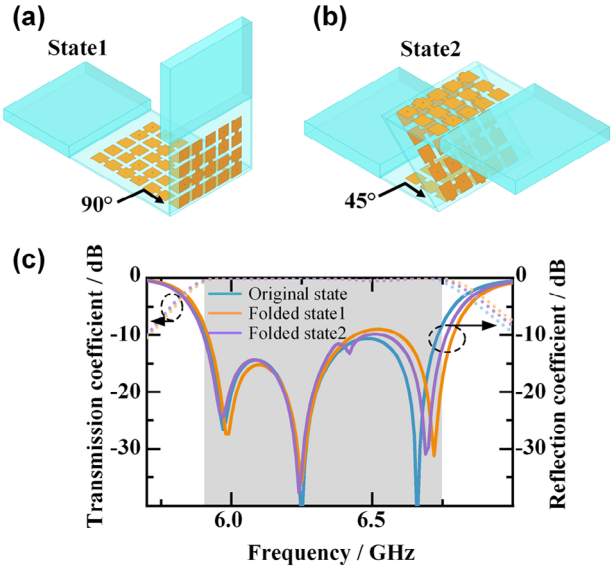

Figure 6. Performance with different geometry states. a) Geometry state 1 and b) state 2 with different folding. c) The simulated transmission and reflection coefficient of the three different geometry states of supercoupling channels with metamaterial.

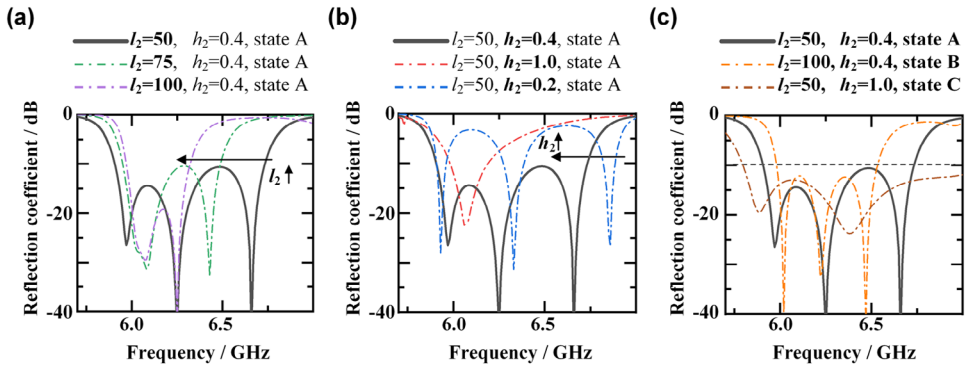

Figure 7. Effect of the key parameter l_2 and h_2 on the supercoupling performance. a) Changing l_2 and b) h_2 on a determined optimized metamaterial state. c) Optimization results on supercoupling channels with different sizes.

for applications in complex or dynamic environments where geometry-independent transmission pathways are essential.

3.3. Parameter Study

In addition to being independent of geometry changes such as folding, the ENZ supercoupling effect is also unaffected by the length of channel. However, the fundamental frequencies of the FP modes are influenced by the length of the supercoupling channels. As shown in **Figure** 7a, the bandwidth of the supercoupling effect varies with the total channel length l_2 for a given optimized metamaterial state. Notably, while l_2 is varied, the metamaterial remains centered within the channel without any structural deformation. It can be observed that as the channel length increases, the resonant frequency of the ENZ mode remains nearly constant, whereas the frequencies of the FP modes decrease, leading to a reduction in the supercoupling bandwidth. Furthermore, consistent with theoretical predictions, the frequency of the FP_2 mode at $l_2 = 100$ mm matches that of the FP_1 mode at $l_2 = 50$ mm. Moreover, the thickness h_2 of the supercoupling channels also significantly affects its performance. As shown in Figure 7b, reducing h_2 decreases the cross-sectional area of the channel, thereby increasing the Q-factor of the ENZ and FP modes, which narrows the bandwidth of the modes and disrupts mode superposition. Conversely, when h_2 becomes relatively large, the cross-sectional area of the channel no longer satisfies the approximation conditions required for ENZ analysis, presenting a single band transmission.

Furthermore, the bandwidth enhancement of supercoupling with inverse-designed metamaterials is validated in various supercoupling channels to demonstrate the universality of proposed method. As shown in Figure 7c, in addition to the optimized states A from Figure 3, the metamaterials are re-optimized for two distinct supercoupling channels with a length of $l_2 = 100$ mm and thickness of $h_2 = 1$ mm, respectively causing the optimized state B and C. The fundamental structural parameters of the metamaterials remain the same as in the previous designs. For state B, the longer channel length caused the resonant frequencies of the FP modes to shift closer to the ENZ mode, resulting in a narrower overall bandwidth. In contrast, state C exhibits a reduced Q-factor because of its larger channel thickness, and further results in a broader optimized bandwidth. Both re-optimized states achieve bandwidth enhancement through multimode superposition, surpassing both the bandwidth achieved by the ENZ mode alone and by metamaterial without re-optimized.

4. Conclusion

As a conclusion, a transformative approach is proposed to overcome the intrinsic bandwidth limitations of ENZ supercoupling by integrating an inverse-designed pixel metamaterial within the ENZ channel. The proposed metamaterials, composed of microscale units, are optimized with a GA method, enabling complex and multifunctional electromagnetic wave control. By integrating the optimized metamaterials into the supercoupling channels, multiple FP resonant modes are precisely controlled, facilitating multimode superposition and achieving substantial bandwidth enhancement. Additionally, the stability of the broadband supercoupling under arbitrary geometry highlights its adaptability for complex transmission environments. Based on the SIW technique, an experimental validation at microwave frequencies demonstrates total transmission over a wide frequency range, confirming the feasibility and robustness of this design in practical devices. By overcoming the inherent narrowband constraint, our approach opens up new avenues for the development of broadband and geometry-independent photonic and electromagnetic devices, with potential impacts spanning telecommunications, sensing, imaging, and quantum technologies.

5. Experimental Section

Method of Momentum: The Method of Moments (MoM) is used to rapidly calculate the transmission and reflection coefficients under different states throughout the optimization process. Treating all k optimizable structures as k ports, the entire supercoupling model can be represented as a circuit model with two feeding ports and k internal equivalent ports. Since the optimized structures are much smaller than the wavelength, their connected and disconnected states can be equivalently modeled as open-circuit and short-circuit states of the equivalent ports. This enables full-wave simulation of a model with 2+k ports, yielding the matrix Z_0 that includes all impedance information. Using Z_0 and the impedance states

of the ports Z_{eq}, the two-port network characteristics Z_{ENZ} of the supercoupling structure can be directly calculated.

$$Z_0 = \begin{bmatrix} Z_{2,2} & Z_{2,k} \\ Z_{K,2} & Z_{k,k} \end{bmatrix} \tag{1}$$

$$Z_{ENZ} = Z_{2,2} + Z_{2,k}\left(Z_{eq} - Z_{k,k}\right)^{-1} Z_{k,2} \tag{2}$$

This port equivalent model accurately describes the actual characteristics of the metamaterial and makes it possible to quickly solve the electromagnetic response for various states.

Optimization Setup with GA: The inverse design process shown in Figure 5 is implemented with MATLAB. There is a total of 204 metamaterial structures that can be optimized. The number of individuals in a single population is 500, with a variation rate of 0.01. When the optimization reaches the expected level, or reaches the maximum number of iterations of 300, or there are no new optimal values for 50 consecutive optimizations, the inverse design algorithm will be stopped. In practical optimization, the objective is set to the sum of the reflection coefficients exceeding −10 dB within the bandwidth of interest. A personal computer is used for optimization, equipped with an Intel (R) Core (TM) i7-10700 CPU @ 2.90 GHz and random-access memory of 64.0 GB.

Numerical Simulation: The structures proposed were modeled and simulated using the Finite Element Method (FEM) in ANSYS HFSS software. Specifically, for the theoretical verification in Figure 3, the following structural parameters were used: $h_1 = 3$ mm, $h_2 = 0.4$ mm, $l_1 = 20$ mm, $l_2 = 50$ mm, $w = 25$ mm. The metamaterial used has 11×5 basic units with the following structural parameters: $r = 0.2$ mm, $a = 3$ mm, $d = 1$ mm, $s = 1$ mm. The waveguide on both sides, with a thickness of 3 mm, has a dielectric constant of 2.65, while the central connecting waveguide is an air-filled waveguide. The sidewalls of the waveguide are set as perfect electric conductors (PEC). Additionally, the cross-sections on both sides of the waveguide are excited using wave ports. The full-wave simulation results provide transmission, reflection, and electromagnetic field distribution states. For the actual model in Figure 4, copper is used as the material with a finite conductivity of $\sigma = 5.8 \times 10^7$ S m^{-1} (same as copper) for the boundary. Detailed dimensions can be found in the Supporting Information. Dielectric board 1 has a permittivity of 6.15 and a loss tangent of 0.0025, while dielectric board 2 has a permittivity of 2.2 and a loss tangent of 0.002. These kinds of permittivity were obtained from the material library in the software. A 50-ohm discrete port was used to excite the position of the SMA connector.

Experimental Setup: The prototype shown in Figure 4 was fabricated with standard PCB manufacturing processes. The top dielectric layer, dielectric 1, is made of Rogers RO3006, while the bottom layer, dielectric 2, Rogers RT5880. The 50-ohm SMA connector has an inner conductor length of 3 mm and is directly connected to the bottom waveguide. Additionally, numerous through-holes, located in the same positions on both the upper and lower waveguides, are used to reinforce the multilayer board with screws. The FieldFox Microwave Analyzer N9951B from KEYSIGHT was used to measure the transmission and reflection coefficients of the structure. The discrepancies between measurements and simulations results are primarily due to fabrication imperfections, such as air gaps, dielectric constant inconsistencies in PCB materials, and additional losses introduced by non-ideal factors.

Supporting Information

Supporting Information is available from the Wiley Online Library or from the author.

Acknowledgements

Y. L. acknowledges the support from National Natural Science Foundation of China (NSFC) under grant U22B2016.

Conflict of Interest

The authors declare no conflict of interest

Data Availability Statement

All data needed to evaluate the conclusions in the paper are present in the paper and/or the Supporting Information. Additional data related to this paper may be requested from Y. Li. (lyee@tsinghua.edu.cn).

Keywords

epsilon-near-zero, inverse design, metamaterials, mode superposition, supercoupling

Received: November 25, 2024
Revised: January 6, 2025
Published online: January 28, 2025

[1] J. Wu, Z. T. Xie, Y. Sha, H. Fu, Q. Li, *Photonics Res.* **2021**, *9*, 1616.
[2] X. Niu, X. Hu, S. Chu, Q. Gong, *Adv. Opt. Mater.* **2018**, *6*, 1701292.
[3] P. Li, W. Yan, S. Wang, P. Fu, Y. Zhang, Y. Li, *Adv. Phys. Res.* **2024**, *3*, 2400070.
[4] Z. Guo, H. Jiang, H. Chen, *J. Phys. D: Appl. Phys.* **2021**, *55*, 083001;
[5] H. Li, Z. Zhou, Y. Zhao, Y. Li, *Chip.* **2023**, *2*, 100049.
[6] Z. Zhou, Y. Li, E. Nahvi, H. Li, Y. He, I. Liberal, N. Engheta, *Phys. Rev. Appl.* **2020**, *13*, 034005.
[7] C. T. DeVault, V. A. Zenin, A. Pors, K. Chaudhuri, J. Kim, A. Boltasseva, V. M. Shalaev, S. I. Bozhevolnyi, *OpticaOptica.* **2018**, *5*, 1557.
[8] Y. Zhang, Y. Li, W. Zhang, Z. Zhang, Z. Feng, *Engineering.* **2022**, *11*, 72.
[9] J. Kim, A. Dutta, G. V. Naik, A. J. Giles, F. J. Bezares, C. T. Ellis, J. G. Tischler, A. M. Mahmoud, H. Caglayan, O. J. Glembocki, *OpticaOptica.* **2016**, *3*, 339.
[10] Y. Zhang, Y. Li, *Electromag. Sci.* **2023**, *1*, 1.
[11] Z. Zhou, Y. Li, *Chinese J. Radio Sci.* **2021**, *36*, 905.
[12] Z. Zhou, H. Li, W. Sun, Y. He, I. Liberal, N. Engheta, Z. Feng, Y. Li, *Light Sci. Appl.* **2022**, *11*, 207.
[13] M. Z. Alam, S. A. Schulz, J. Upham, I. De Leon, R. W. Boyd, *Nat. Photonics.* **2018**, *12*, 79.
[14] O. Reshef, I. De Leon, M. Z. Alam, R. W. Boyd, *Nat. Rev. Mater.* **2019**, *4*, 535.
[15] C. Wang, R. Shi, L. Gao, A. S. Shalin, J. Luo, *Photonics Res.* **2023**, *11*, 1437.
[16] H. Ma, Y. Zhao, Y. Shao, Y. Lian, W. Zhang, G. Hu, Y. Leng, J. Shao, *Photonics Res.* **2021**, *9*, 678.
[17] J. Park, J.-H. Kang, X. Liu, M. L. Brongersma, *Sci. Rep.* **2015**, *5*, 15754.
[18] H. Li, P. Fu, Z. Zhou, W. Sun, Y. Li, J. Wu, Q. Dai, *Sci. Adv.* **2022**, *8*, eabq6198.
[19] M. Silveirinha, N. Engheta, *Phys. Rev. Lett.* **2006**, *97*, 157403.
[20] M. G. Silveirinha, N. Engheta, *Phys. Rev. B.* **2007**, *76*, 245109.
[21] Y. Li, N. Engheta, *Phys. Rev. B.* **2014**, *90*, 201107.
[22] A. Alù, M. G. Silveirinha, N. Engheta, *Phys. Rev. E.* **2008**, *78*, 016604.
[23] S. Zhong, J. Feng, Z. W. Zheng, Y. Ma, *Propag. Lett.* **2022**, *21*, 1896.
[24] B. Edwards, A. Alù, M. E. Young, M. Silveirinha, N. Engheta, *Phys. Rev. Lett.* **2008**, *100*, 033903.
[25] R. Liu, Q. Cheng, T. Hand, J. J. Mock, T. J. Cui, S. A. Cummer, D. R. Smith, *Phys. Rev. Lett.* **2008**, *100*, 023903.
[26] R. Liu, C. M. Roberts, Y. Zhong, V. A. Podolskiy, D. Wasserman, *ACS Photonics.* **2016**, *3*, 1045.
[27] E. J. R. Vesseur, T. Coenen, H. Caglayan, N. Engheta, A. Polman, *Phys. Rev. Lett.* **2013**, *110*, 013902.

[28] M. H. Javani, M. I. Stockman, *Phys. Rev. Lett.* **2016**, *117*, 107404.
[29] W. Yan, Z. Zhou, H. Li, Y. Li, *Nat. Commun.* **2023**, *14*, 6154.
[30] W. Yan, Z. Zhou, H. Li, W. Sun, Q. Lv, Y. Li, *Laser Photonics Rev.* **2023**, *17*, 2201000.
[31] S. Hrabar, I. Krois, A. Kiricenko, *Metamaterials.* **2010**, *4*, 89.
[32] M. Mitrovic, B. Jokanovic, N. Vojnovic, *Propag. Lett.* **2013**, *12*, 631.
[33] Y. He, Y. Li, Z. Zhou, H. Li, Y. Hou, S. Liao, P. Y. Chen, *Adv. Theor. Simul.* **2019**, *2*, 1900059.
[34] Y. Yang, Y. Liu, J. Qin, S. Cai, J. Su, P. Zhou, L. Deng, Y. Li, L. Bi, *Photonics Res.* **2023**, *11*, 1613.
[35] J. Dai, H. Jiang, Z. Guo, J. Qiu, *Adv. Funct. Mater.* **2024**, *34*, 2308338;
[36] J. R. Hendrickson, S. Vangala, C. Dass, R. Gibson, J. Goldsmith, K. Leedy, D. E. Walker Jr, J. W. Cleary, W. Kim, J. Guo, *ACS Photonics.* **2018**, *5*, 776.
[37] X. Qin, Y. Li, *Phys. Rev. Appl.* **2021**, *16*, 024033.
[38] T. J. Cui, S. Zhang, A. Alù, M. Wegener, J. Pendry, J. Luo, Y. Lai, Z. Wang, X. Lin, H. Chen, *J. Phys.: Photonics.* **2024**, *6*, 032502.
[39] T. J. Cui, L. Li, S. Liu, Q. Ma, L. Zhang, X. Wan, W. X. Jiang, Q. Cheng, *Iscience.* **2020**, *23*, 101403.
[40] Y. Dong, T. Itoh, *Proc. IEEE.* **2012**, *100*, 2271.
[41] P. Fu, Z. Xu, T. Zhou, H. Li, J. Wu, Q. Dai, Y. Li, *Nat. Commun.* **2024**, *15*, 6258.
[42] W. J. Padilla, R. D. Averitt, *Nat. Rev. Phys.* **2022**, *4*, 85.
[43] I. Staude, J. Schilling, *Nat. Photonics.* **2017**, *11*, 274.
[44] K. Y. Yang, C. Shirpurkar, A. D. White, J. Zang, L. Chang, F. Ashtiani, M. A. Guidry, D. M. Lukin, S. V. Pericherla, J. Yang, *Nat. Commun.* **2022**, *13*, 7862.
[45] X. Qin, P. Fu, W. Yan, S. Wang, Q. Lv, Y. Li, *Nat. Commun.* **2023**, *14*, 7041.
[46] L. Sun, Y. Lin, K. W. Yu, G. P. Wang, *New J. Phys.* **2022**, *24*, 073016.
[47] R. Calpe, P. Karvinen, P. Pääkkönen, M. Ornigotti, H. Caglayan, J. Turunen, T. K. Hakala, M. Koivurova, *Appl. Phys. Lett.* **2024**, *124*, 073016.
[48] M. Koivurova, T. Hakala, J. Turunen, A. T. Friberg, M. Ornigotti, H. Caglayan, *New J. Phys.* **2020**, *22*, 093054.
[49] M. A. Castillo, C. Estévez-Varela, W. P. Wardley, R. Serna, I. Pastoriza-Santos, S. Núñez-Sánchez, M. Lopez-Garcia, *Adv. Funct. Mater.* **2022**, *32*, 2113039.